Inverse-designed 3D sequential metamaterials achieving extreme stiffness

Han, Jiacheng; Zhai, Xiaoya; Wang, Lili; Zhang, Di; Ding, Junhao; Ma, Winston Wai Shing; Song, Xu; Liao, Wei Hsin; Liu, Ligang; Wu, Jun

Important note
To cite this publication, please use the final published version (if applicable).
Please check the document version above.

Inverse-designed 3D sequential metamaterials achieving extreme stiffness

Jiacheng Han [a], Xiaoya Zhai [a,*], Lili Wang [a], Di Zhang [a], Junhao Ding [b], Winston Wai Shing Ma [b], Xu Song [b], Wei-Hsin Liao [b], Ligang Liu [a], Jun Wu [c], Xiao-Ming Fu [a]

[a] School of Mathematical Sciences, University of Science and Technology of China, Hefei, Anhui, China
[b] Department of Mechanical and Automation Engineering, The Chinese University of Hong Kong, Hong Kong, China
[c] Department of Sustainable Design Engineering, Delft University of Technology, Delft, the Netherlands

ARTICLE INFO

ABSTRACT

Mechanical metamaterials signify a groundbreaking leap in material science and engineering. The intricate and experience-dependent design process poses a challenge in uncovering architectural material sequences with exceptional mechanical properties. This study introduces inverse-designed 3D sequential metamaterials with outstanding mechanical attributes, achieved through a novel computational framework. The explored sequences based on Schoen's I-graph–wrapped package (IWP) and Schwarz Primitive (Schwarz P) surpass the Hashin-Shtrikman upper bound of Young's modulus at relative densities of 0.24 and 0.43, outperforming previous records. Optimized Body-Centered-Cubic (BCC) truss-based sets outperform traditional ones by 72.7%. This innovative approach can be extended for metamaterial customization, involving the optimization of multi-directional Young's modulus, total stiffness, and the addition of isotropy constraints. The paper explores the characteristics and implications of this innovation, emphasizing the impact of geometric and topological variations on mechanical performance. These metamaterial sequences offer unparalleled adaptability, and hold significant potential in structural engineering and adaptive mechanical systems, opening avenues for technological advancements.

1. Introduction

Mechanical metamaterials are engineered to exhibit specific and unconventional mechanical behaviors. They are highly adaptable and exhibit exceptional mechanical properties, such as ultralight weight [1,2], high strength [3,4], and excellent energy absorption [5,6]. Their performance can also be customized through mechanical symmetries [7,8], buckling resistance [9,10], and other advanced structural behaviors. Moreover, nature has served as a key inspiration for mechanical metamaterial designs, such as those derived from bamboo [11] and deep-sea sponges [12], resulting in optimized, hierarchical architectures. Two-dimensional (2D) mechanical metamaterials have been widely explored until now [13–16], but there is an increasing demand for three-dimensional (3D) metamaterials in the real world. For metamaterials, both customization properties [17,18], enabling the generation of desired properties, and sequential metamaterials [19–21], ensuring the controllability of properties, are critical aspects. Moreover, exploring materials at their mechanical limits [22–24] is also highly important

because of the potential for structures to achieve extreme stiffness, allowing them to be exceptionally stiff while also being lightweight.

Despite the critical applications and great potential of 3D metamaterials, designing metamaterials that meet the above requirements (customized, sequential, and achieving extreme mechanical properties) still faces a significant challenge. For metamaterials design, existing approaches involve empirical design [25–27], nature inspired methods [28–33], theoretical design [2,22,34], and topology optimization [35,36]. Empirical and nature-inspired design methods involve extensive observation and iterative refinement, often resulting in lengthy design cycles. The theoretical design method [2,22,34] offers assurance of theoretical validity but provides limited geometric and topological information. In contrast, topology optimization [37–43] serves as an inverse design approach capable of addressing the aforementioned issues. Topology optimization can also be extended to 3D metamaterials but faces a trade-off between computational efficiency and calculation accuracy. Despite this, work [44] developed a large-scale metamaterial design framework. Recently, artificial intelligence (AI), particularly deep learning, has emerged as a powerful tool in 3D metamaterial de-

sign [45,46]. AI can replace parts of traditional finite element calculations, significantly accelerating the simulation of physical properties and the inverse optimization process [47]. Furthermore, generative models enable the creation of mechanical metamaterial designs that meet specific performance criteria, offering a faster and more efficient approach to developing high-performance structures [48,49]. However, previous studies [2,4,22,23,26,27,34,50–52] have primarily emphasized the characteristics of individual metamaterials, with limited discussion on the consistency of geometric and physical properties in 3D sequential metamaterials.

Sequential metamaterials can be crafted with tunable properties, enabling meticulous control of their behavior. The tunable characteristics of metamaterial sequences manifest in certain physical properties, including density, Young's modulus, and others. Specifically, metamaterial sequences exhibit an increasing Young's modulus. The generation of microstructure sequences can be categorized into non-uniform deformation methods [33,53,54] and geometric interpolation methods [55,56]. These algorithms focus on ensuring connectivity between neighboring microstructures. Other relevant methods [57,58] not only consider microstructure connectivity but also emphasize the compatibility of physical properties, aiming to generate sequences that closely approach the theoretical upper limit. However, they perform discrete interpolation and do not allow for generating a continuous microstructure sequence. In comparison, this paper aims to delve into geometric connectivity and physical compatibility while aspiring to generate a continuous 3D microstructure sequence to ensure meticulous material fine-tuning.

The design of metamaterials, particularly those aimed at achieving extreme mechanical properties, represents a crucial yet challenging avenue in mechanics research. The Hashin-Shtrikman (HS) upper bounds [59] play a pivotal role in composite materials, establishing theoretical limits on stiffness for isotropic material design. By employing heuristic approaches and both qualitative and quantitative analyses, an isotropic plate lattice composed of closed-cell cubic foam and octet foam is found to attain the HS upper bounds [22]. The introduction of a plate-lattice structure between two adjacent trusses, known as octet-plate structures, demonstrated closer proximity to the HS upper bound, compared to octet-truss structures [23]. However, due to the closed-cell nature of plate lattices, manufacturing challenges exist. Inspired by surface curvature-driven strategies observed in natural soap films and by mimicking the expanding soap film concept for the natural occupation of periodic volumes, shell-based mechanical metamaterials overcome production challenges, although there still exists a 6% gap from the HS upper bound at medium densities [33]. Microlattices based on IWP and Neovius topologies, while exhibiting superior modulus and strength, but lack customization and tunability [4]. Despite numerous design principles and strategies emerging from current research, only a limited number of materials capable of reaching high-stiffness limits, especially those featuring customized and tunable sequences, have been identified.

This paper proposes a comprehensive framework designed for generating metamaterial sequences while approaching extreme stiffness. Various classes of metamaterial sequences, including shell, truss, and plate architectures, are constructed for three key features: customization, tunability, and extremely high stiffness. Our findings indicate that IWP-based metamaterial sequences can surpass the HS upper bound of Young's modulus at a relative density of 0.24. Furthermore, we have identified a series of continuously evolving metamaterials, starting with the Schwarz P structure, that outperform the HS upper bound of Young's modulus at the relative density of 0.43. The sequences generated by our framework exhibit enhanced properties, with BCC truss-based metamaterial sequences experiencing the most substantial improvement up to 72.7% than those obtained by traditional offset operations. The enhancement of shell-based structures is primarily observed in reaching the HS upper bound of Young's modulus at the low relative density. All the data referenced in this paper can be downloaded from https://github.com/JiachengHan1025/Inverse3Dmetamaterials. This paper elucidates the framework by characterizing the optimiza-

tion process as a non-uniform heat diffusion process, as shown in Fig. 1, with the candidate cell as the heat source. The proposed framework can also customize the mechanical behavior of a structure by changing the objective function. Rigorous simulations and experimental tests are conducted to validate and demonstrate the efficacy of the proposed framework.

2. Methods

To formulate a collection of 3D metamaterials, we introduce a methodology characterized by non-uniform heat diffusion. The process begins with selecting a voxel-based structure as a candidate cell, designated as the heat source for heat diffusion. Varying heat diffusion coefficients α yield distinct temperature fields T. By extracting isosurfaces of temperature field at a specific value and considering voxels with temperatures less than or equal to that value as solid, each isosurface corresponds to a microstructure. By adjusting this value, we can decode a sequence of microstructures from the temperature field. As candidate cells, we have chosen microstructures based on shells, plates, and trusses, as illustrated in Fig. 1. Three elastic moduli, namely Young's modulus (E), bulk modulus (K), and shear modulus (G), serve as the objective functions for optimization. In the following sections, the sequence obtained through optimization, with structure S as the candidate cell and modulus M as the objective function, is designated as the Opt $S - M$ sequence.

Given the design domain $\Omega = [0,1]^3$ and a candidate cell ρ_0, a heat diffusion coefficient field α need be optimized targeting at different objectives. We utilize ρ_0 as a constant temperature heat source for optimized heat diffusion, which leads to a continuous temperature field τ. By taking different iso-surfaces of τ, we can obtain a microstructure sequence that is geometrically continuous. Changing α correspondingly induces changes in the microstructure sequences. To obtain a microstructure sequence with extreme mechanical properties, we use topology optimization based on finite element discretization to solve the microstructure sequence optimization problem. The corresponding optimization process can be seen in Fig. S1.

2.1. Formulation

ρ_0 is represented as a binary field, meaning that for $\forall x \in \Omega$, $\rho_0(x) \in \{0,1\}$. We discretize Ω into N elements, with each element e with a volume fraction of v_e. We assign a heat diffusion coefficient α_e to each element e, and by sampling the iso-surfaces of the temperature field, we obtain M distinct key microstructures $\rho^1, \cdots, \rho^M$. We use the mechanical properties of these M microstructures as our optimization objectives. The optimization model is as follows:

$$\max_{\alpha} \quad J(\alpha) = \sum_{m=1}^{M} f\left(E^H(\rho^m)\right),$$
$$\text{s.t.} \quad A(\alpha)T = T_0,$$
$$V(\rho^m) = \frac{\sum_{n=1}^{N} v_e \rho_e^m}{|\Omega|} \leq V^m, \quad m = 1, \cdots, M;$$
$$0 \leq \alpha_e \leq 1, \quad \forall e;$$

where $f\left(E^H(\rho)\right)$ represents the mechanical properties determined by the effective elastic tensor $E^H(\rho)$ of the structure ρ. The effective elastic tensor is calculated by the numerical homogenization method. $A(\alpha)T = T_0$ represents the discretized state equation for the heat diffusion equation. V^m corresponds to the preset volume constraint for the m-th key microstructure.

2.2. Solving heat diffusion equation

The 3D heat diffusion equation is shown in the following:

$$\frac{\partial}{\partial x}\left(\alpha \frac{\partial T}{\partial x}\right) + \frac{\partial}{\partial y}\left(\alpha \frac{\partial T}{\partial y}\right) + \frac{\partial}{\partial z}\left(\alpha \frac{\partial T}{\partial z}\right) = \frac{\partial T}{\partial t}, \quad (x,y,z) \in \Omega;$$
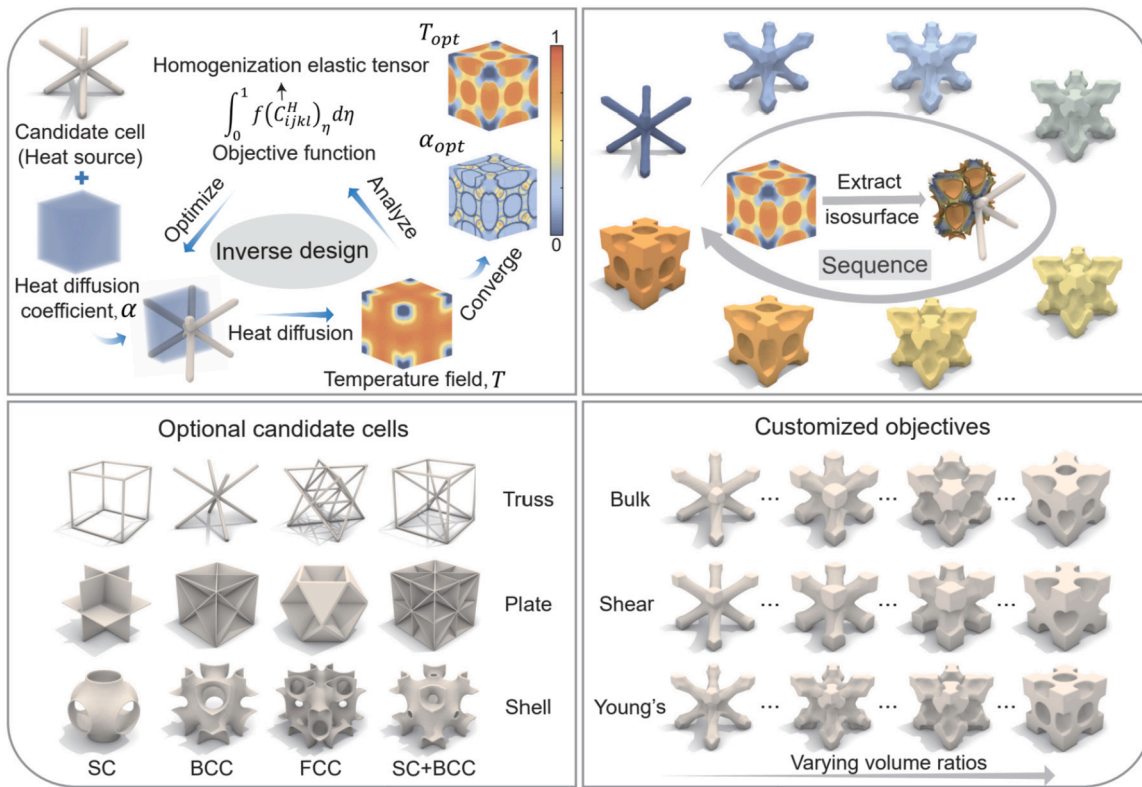
Fig. 1. Illustration of the optimization framework. As a candidate cell, the BCC truss is the heat source for heat diffusion. The obtained temperature field can decode a sequential microstructure. After conducting mechanical analysis on the sequential microstructure, the heat diffusion coefficient can be optimized to maximize the objective function (top left). Decoding a sequential microstructure from the temperature field involves specifying a value, extracting the iso-surface from the temperature field, and considering voxels below that value as the corresponding microstructure (top right). The candidate cell can be arbitrarily chosen, such as truss, plate, or shell structures (bottom left). The objective function f can be selected as bulk modulus, shear modulus, Young's modulus, and the optimized sequence varies accordingly (bottom right).

The left-hand side of the equation is discretized using finite element methods, while the right-hand side is discretized using finite difference methods, yielding the discretized heat diffusion equation:

$$K^{heat}(\alpha)T_{\Delta t} = \frac{T_{\Delta t} - T_0}{\Delta t},$$

where T_0 represents the temperature field at the initial time, $T_{\Delta t}$ represents the temperature field at time Δt, and $K^{heat}(\alpha)$ is the stiffness matrix of the heat diffusion equation, which can be assembled from the matrix of element K_e^{heat}.

$$K^{heat}(\alpha) = \sum_e \alpha_e K_e^{heat} \longrightarrow (I - \Delta t K^{heat}(\alpha))T_{\Delta t} = T_0.$$

We can obtain the temperature field $\tilde{T} = T_{\Delta t}$ on the nodes, and get $A(\alpha) = (I - \Delta t K^{heat}(\alpha))T_{\Delta t}$. For the temperature values $\bar{T}_e$ on element e, we calculate it by averaging the temperature values of the eight nodes of the element:

$$\bar{T}_e = \frac{1}{8}\sum_{node \in e} \tilde{T}_{node}.$$

This allows us to obtain the temperature field $\bar{T}$ on the elements. We can express the above transformation in a linear form as follows:

$$\bar{T} = G \cdot \tilde{T}.$$

Subsequently, we use $\bar{T}$ to generate microstructure sequence and key microstructures.

2.3. Homogenization method

The effective mechanical properties of microstructure can be calculated by the homogenization method. Considering a structure ρ on the domain Ω, the effective elastic tensor E_{ijkl}^H of the microstructure which is obtained by periodically tiling it, can be calculated using the following formula:

$$E_{ijkl}^H = \frac{1}{|\Omega|} \int_\Omega \left(\varepsilon_{pq}^{0(ij)} - \varepsilon_{pq}^{(ij)}\right) E_{pqrs} \left(\varepsilon_{rs}^{0(kl)} - \varepsilon_{rs}^{(kl)}\right) d\Omega,$$

where ε_{ij}^0 represents the unit test strain fields, and ε_{ij} represents the periodic fluctuation fields, which can be obtained by solving the following elastic equation:

$$\int_\Omega E_{ijpq}\varepsilon_{pq}^{(kl)}\frac{\partial v_i}{\partial y_i}dY = \int_\Omega E_{ijpq}\varepsilon_{pq}^{0(kl)}\frac{\partial v_i}{\partial y_i}d\Omega,$$

where v is a virtual displacement field. Using the finite element method, we discretize Ω into N elements, and the corresponding element stiffness matrix is given by $K_e = E_e(\rho_e)K_0$. For grayscale elements, we utilize the SIMP interpolation method:

$$E_e(\rho_e) = E_{\min} + \rho_e^p (E_0 - E_{\min}).$$

The discretized calculation of E^H is given by:

$$E_{ijkl}^H = \frac{1}{|\Omega|}\sum_{e=1}^N \left(\mathbf{u}_e^{0(ij)} - \mathbf{u}_e^{(ij)}\right)^T K_e \left(\mathbf{u}_e^{0(kl)} - \mathbf{u}_e^{(kl)}\right).$$

The corresponding sensitivity analysis is as follows:

$$\frac{\partial E^H_{ijkl}}{\partial \rho_e} = \frac{1}{|\Omega|} p \cdot \rho_e^{p-1} \left(E_0 - E_{\min} \right) \left(\mathbf{u}_e^{0(ij)} - \mathbf{u}_e^{(ij)} \right)^T K_e \left(\mathbf{u}_e^{0(kl)} - \mathbf{u}_e^{(kl)} \right).$$

2.3.1. Calculation details

Filtering We filter the heat diffusion coefficient before heat diffusion to obtain the filtered heat diffusion coefficient field $\tilde{\alpha}$, which helps prevent the checkerboard pattern. The filter process is carried out using a common density formula in topology optimization, as follows:

$$\tilde{\alpha}_e = \frac{\sum_{i \in N_e} \omega_e(x_i, r) v_i \alpha_i}{\sum_{i \in N_e} \omega_e(x_i, r) v_i},$$

Here, r is the filtering radius, N_e represents the neighboring elements of e, defined as $N_e = \{ i \mid \|x_i - x_e\| \leq r \}$, and the filtering weight is given by $\omega_e(x_i, r) = r - \|x_i - x_e\|$. Because $\tilde{\alpha}$ and α have a linear transformation relationship, the transformation between them can be expressed as:

$$\tilde{\boldsymbol{\alpha}} = H \cdot \boldsymbol{\alpha},$$

Correspondingly, the discretized state equation for the heat diffusion equation becomes

$$A(\tilde{\alpha}) T = T_0.$$

Iso-surface sampling After obtaining the filtered heat diffusion coefficient field $\tilde{\alpha}$ and solving the heat diffusion using the method in Section 2, we obtain the temperature field $\bar{T}$. If we want to associate the density field with the extracted μ-iso-surfaces of the temperature field, we can employ a smoothing projection technique. For instance, with a given truncation threshold $\mu \in [0, 1]$, when the temperature $\bar{T}_e \geq \mu$, we set the density ρ_e to 0; when the temperature $\bar{T}_e < \mu$, we set the density ρ_e to 1. However, this projection method isn't convenient for the sensitivity analysis. Through the following smooth projection function, we can project the temperature T_e on element e to the density ρ_e:

$$\rho_e = \mathbf{P}(\beta, \mu, T_e) = \frac{\tanh(\beta\mu) + \tanh(\beta(T_e - \mu))}{\tanh(\beta\mu) + \tanh(\beta(1 - \mu))},$$

here, β is the projection coefficient. A larger β makes the projected density field ρ approach binary values more closely. By providing M projection thresholds $\mu_1, \dots, \mu_M$, we can use the projection function to obtain the corresponding M key microstructures $\rho^1, \dots, \rho^M$. To make iterations stable, we initialize β with a small value, such as 16. Subsequently, we double its value every 50 iterations.

Volume constraint Assuming the maximum volume for the key microstructures is V^{max}, we uniformly sample between the candidate cell's volume $V(\rho^0)$ and V^{max}. In other words:

$$V^m = V(\rho^0) + \frac{V^{max} - V(\rho^0)}{M} m, \quad m = 1, \dots, M;$$

The projection threshold μ_m is related to V^m through the following linear relationship:

$$\mu_m = \frac{V^m - V(\rho^0)}{1 - V(\rho^0)}.$$

Cubic symmetry To ensure the resulting sequence possesses cubic symmetry, the candidate cell, denoted as ρ_0, should inherently be cubic symmetry. Additionally, following each iterative update, we perform symmetrical operations on the heat diffusion coefficient field $\boldsymbol{\alpha}$. Specifically, we extract the heat diffusion coefficient field $\boldsymbol{\alpha}^{part}$ from the $\frac{1}{48}$ tetrahedra contained within the cube Ω and subject it to symmetrical transformations across nine planes. This process ensures that the temperature field obtained during each iteration exhibits symmetry across these nine planes. Consequently, the resulting microstructure sequence possesses cubic symmetry.

Isotropy constraints To ensure that the generated microstructure sequence is as isotropic as possible, we apply isotropy constraints to the key microstructures. Assuming the zener ratio of the key microstructure ρ^m is ξ_m, and given an isotropy control threshold of ε_{iso}, the corresponding optimization model becomes:

$$\begin{aligned} \max_{\boldsymbol{\alpha}} \quad & J(\boldsymbol{\alpha}) = \sum_{m=1}^{M} f\left(E^H(\rho^m) \right), \\ \text{s.t.} \quad & A(\tilde{\alpha}) T = T_0, \\ & \xi_m \leq \varepsilon_{iso} \quad m = 1, \dots, M; \\ & V(\rho^m) = \frac{\sum_{n=1}^{N} v_e \rho_e^m}{|\Omega|} \leq V^m \quad m = 1, \dots, M; \\ & 0 \leq \alpha_e \leq 1, \quad \forall e. \end{aligned}$$

Channel constraints If we intend to preserve the open-cell nature of the generated sequence, channel constraints can be added at potential closed-cell locations. This entails setting the heat diffusion coefficient of the voxels within the channels to 0 and, likewise, setting the corresponding derivatives to 0 during sensitivity analysis.

2.3.2. Sensitivity analysis

In general, considering a function $h(\rho)$, according to the chain rule, we have:

$$\frac{\partial h}{\partial \alpha_e} = \sum_{j \in N_e} \frac{\partial h}{\partial \rho} \cdot \frac{\partial \rho}{\partial \bar{T}} \cdot \frac{\partial \bar{T}}{\partial \tilde{T}} \cdot \frac{\partial \tilde{T}}{\partial \tilde{\alpha}_j} \cdot \frac{\partial \tilde{\alpha}_j}{\partial \alpha_e},$$

$\frac{\partial \rho}{\partial \bar{T}}$ can be derived from the projection function formula, while $\frac{\partial \bar{T}}{\partial \tilde{T}}$ and $\frac{\partial \tilde{\alpha}_j}{\partial \alpha_e}$ can be obtained from the respective linear transformation formulas.

For $\frac{\partial h}{\partial \tilde{\alpha}_j}$, we can solve it using the adjoint method. Given an arbitrary vector λ, we have $h = h + \lambda^T (A(\tilde{\alpha}) \tilde{T} - T_0)$, and as a result:

$$\begin{aligned} \frac{\partial h}{\partial \tilde{\alpha}_j} &= \frac{\partial h}{\partial \tilde{\alpha}_j} + \lambda^T \left(\frac{\partial A(\tilde{\alpha})}{\partial \alpha_j} \tilde{T} + A(\tilde{\alpha}) \frac{\partial \tilde{T}}{\partial \tilde{\alpha}_j} \right) \\ &= \frac{\partial h}{\partial \tilde{T}} \frac{\partial \tilde{T}}{\partial \tilde{\alpha}_j} + \lambda^T \left(\frac{\partial A(\tilde{\alpha})}{\partial \alpha_j} \tilde{T} + A(\tilde{\alpha}) \frac{\partial \tilde{T}}{\partial \tilde{\alpha}_j} \right) \\ &= \left(\frac{\partial h}{\partial \tilde{T}} + \lambda^T A(\tilde{\alpha}) \right) \frac{\partial \tilde{T}}{\partial \tilde{\alpha}_j} + \lambda^T \frac{\partial A(\tilde{\alpha})}{\partial \tilde{\alpha}_j} \tilde{T}. \end{aligned}$$

By setting $\frac{\partial h}{\partial \tilde{T}} + \lambda^T A(\tilde{\alpha}) = 0$ and solving for the corresponding λ, we obtain:

$$\frac{\partial h}{\partial \tilde{\alpha}_j} = \lambda^T \frac{\partial A(\tilde{\alpha})}{\partial \tilde{\alpha}_j} \tilde{T},$$

where

$$\frac{\partial A(\tilde{\alpha})}{\partial \tilde{\alpha}_j} = -\Delta t \frac{\partial K(\tilde{\alpha})}{\partial \tilde{\alpha}_j} = -\Delta t K_e.$$

In our model, $\frac{\partial f(E^H(\rho^m))}{\partial \rho^m}$ can be calculated using the inverse homogenization formula, and the components of $\frac{\partial V(\rho^m)}{\partial \rho^m}$ can be computed as $\frac{\partial V(\rho^n)}{\partial \rho_e^n} = \frac{v_e}{|\Omega|}$.

2.4. Optimization process

We utilize the MMA (Moving Asymptotes Method) for iterative optimization of the model. The procedure for each iteration is as follows:
(1) Using the candidate cell ρ_0 and the heat diffusion coefficient field $\boldsymbol{\alpha}$, the temperature field $\bar{T}$ on the elements is obtained.
(2) By sampling $\bar{T}$, we obtain M distinct key microstructures, denoted as $\rho^1, \dots, \rho^m$.
(3) We calculate the volume of the key microstructures and determine their target mechanical properties using the homogenization method.
(4) Through sensitivity analysis, we compute $\frac{\partial J(\boldsymbol{\alpha})}{\partial \alpha_e}$ and $\frac{\partial V(\rho^m)}{\partial \alpha_e}$.
(5) We use the MMA method to iteratively update $\boldsymbol{\alpha}$.
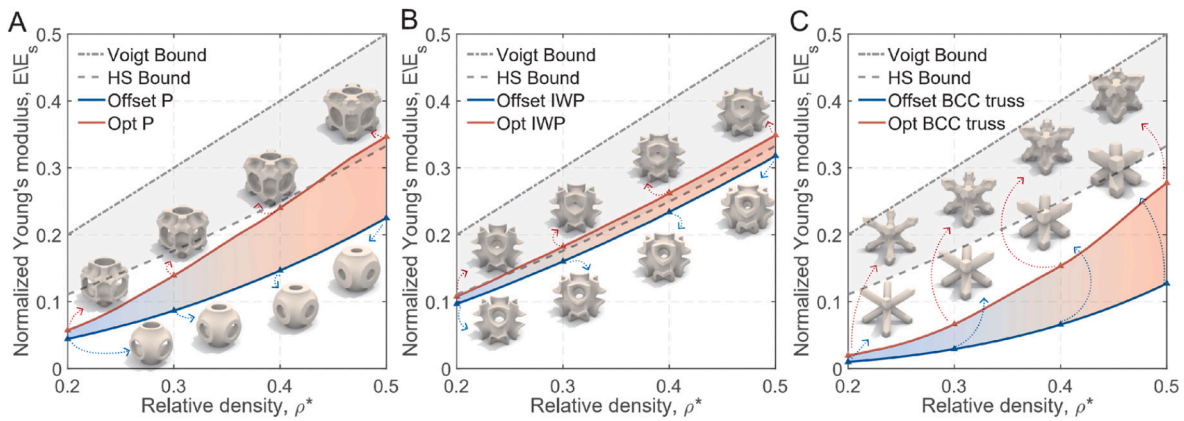
Fig. 2. Illustration and optimization results of the non-uniform deformation algorithm based on heat diffusion. Using Schwarz P (A), IWP (B), and BCC truss (C) as candidate cells and Young's modulus as the objective function, we compare Young's modulus of the optimized sequences with those obtained directly from the uniform thickness offset.

3. Results

3.1. Achieving extreme stiffness

This study presents several 3D sequential metamaterials with extreme stiffness, which have seldom been reported in previous studies of metamaterial topology optimization or cell-based optimization. Due to the inherently high stiffness of plate structures, the optimization space is limited. Therefore, truss and shell-based structures are chosen as candidate cells for optimization to demonstrate the superiority of our algorithm. The proposed metamaterial sequences, optimized based on the Schwarz P, IWP, BCC truss, and Simple-Cubic (SC) truss structures, exhibit obvious improvement in various elastic moduli compared to their counterparts generated by direct uniform offset operations. The initial Schwarz P and IWP are generated through Surface Evolver software [60] and subsequent voxelization.

In Fig. 2A-C, the Opt IWP-Young's sequence reached the HS upper bound at a relative density of $\rho^* = 0.24$, while Opt Schwarz P-Young's sequence reached the HS upper bound at a relative density of $\rho^* = 0.43$. In the optimization process of the IWP here, channel constraints have been introduced to ensure open-cell characteristics, as illustrated by the IWP with constraint 1 in Fig. S3A. This operation facilitates subsequent manufacturing, as demonstrated in the simulation and verification section. In Fig. 3A, we have identified several metamaterials approaching the extreme Young's modulus. Fig. 3B depicts the temperature field T obtained by optimizing the IWP and Schwarz P as the candidate cells; the different colors in the figure represent the iso-surfaces of the temperature field. In Fig. 3C-H, our algorithm significantly enhances various elastic moduli with increasing ρ^*. The Young's modulus of the Opt BCC truss-Young's sequence can be improved by 72.7% compared with that of the sequence obtained by the traditional uniform offset operation. Furthermore, it is worth noting that all optimized sequences possess cubic symmetry and exhibit identical bulk moduli along different directions. Therefore, they cannot surpass the HS upper bounds of bulk modulus for isotropic elastic solids (Fig. 3E). In contrast, lattices with cubic symmetry generally possess anisotropic Young's and shear moduli, and can surpass the HS upper bounds of Young's and shear moduli through the appropriate design of internal microarchitectures (Fig. 3C,D). The optimized sequences and the corresponding temperature fields from Fig. 4 are provided in Figs. S4-S6.

3.2. Simulation and verification

To further demonstrate the stiffness of the structure, simulations and manufacturing validation were conducted using the Opt Schwarz P-Young's sequence (Fig. 4A) and Opt IWP-Young's sequence (Fig. 4B) as examples.

Fabrication The dimensions of all fabricated samples are 15 mm × 15 mm × 15 mm. A laser powder bed fusion printer, Han's Laser M100, equipped with a 500 W IPG fiber laser with a beam diameter of 25 μm was used for metallic lattice manufacturing. SS316L stainless steel powder with a size range of 5 to 23 μm and an average particle size of 15 μm (D50 = 15 μm) was used. Nitrogen inert gas was used to maintain the oxygen concentration below 500 ppm. The processing settings are configured as follows: a laser power of 50 W, a hatch spacing of 50 μm, a scanning speed of 1000 mm/s, and a layer thickness of 10 μm. The commercial software Materialise Magics was used to process the models and generate toolpaths.

Simulation The structure based on voxel representation is first transformed into a smooth mesh. For each model, the ratio of the average mesh edge length to the unit cell edge length is approximately 0.025. The STL files used for the simulations are provided in the supplementary files. Subsequently, the mesh underwent tetrahedralization and discretization into C3D10M elements. Finally, the mesh was imported into Abaqus for finite element simulation, where the periodic boundary conditions for the unit cell were applied using the EasyPBC [61] plugin.

Experiments The elastic modulus was evaluated by a loading-unloading compressive test within the linear elastic range using an MTS810 universal test machine. The displacement of the compression head was measured by Crack Opening Displacement (COD) gauges, and the nominal strain rate was set as $10^{-3}/s$.

Fig. 4C illustrates the strain energy distribution for the Opt Schwarz P-Young's sequence with periodic boundary condition (PBC) of uniaxial compression. As the relative density increases, more strain energy is stored in the middle part of the Opt Schwarz P-Young's sequence, which corresponds to the zoomed-in part in Fig. 4C. This is because, through our framework's optimization of Young's modulus in the vertical direction, the structure tends to locally form a vertical plate-like structure in certain regions. Similarly, as shown in Fig. 4D, there is a similar tendency emerging in the corner of the Opt IWP-Young's sequence.

Models for the Opt Schwarz P-Young's sequence and Opt IWP-Young's sequence at relative densities of 0.2, 0.3, 0.4, and 0.5 were fabricated. These are illustrated in Figs. 4E and 4F, respectively. Physical experiments have been methodically conducted, and the elastic modulus was evaluated by the loading-unloading compressive test [62]. The stress-strain curves are shown in Fig. 4G and Fig. 4I. The initial loading curve often exhibits a small slope, mostly due to the presence of non-flat surfaces. Hence, Young's modulus was calculated based on the linear portion of the stress-strain curve. In Fig. 4H and Fig. 4J, the blue triangle dots signify the outcomes of the experimental test, while the blue square dots denote the results obtained from numerical simulations.
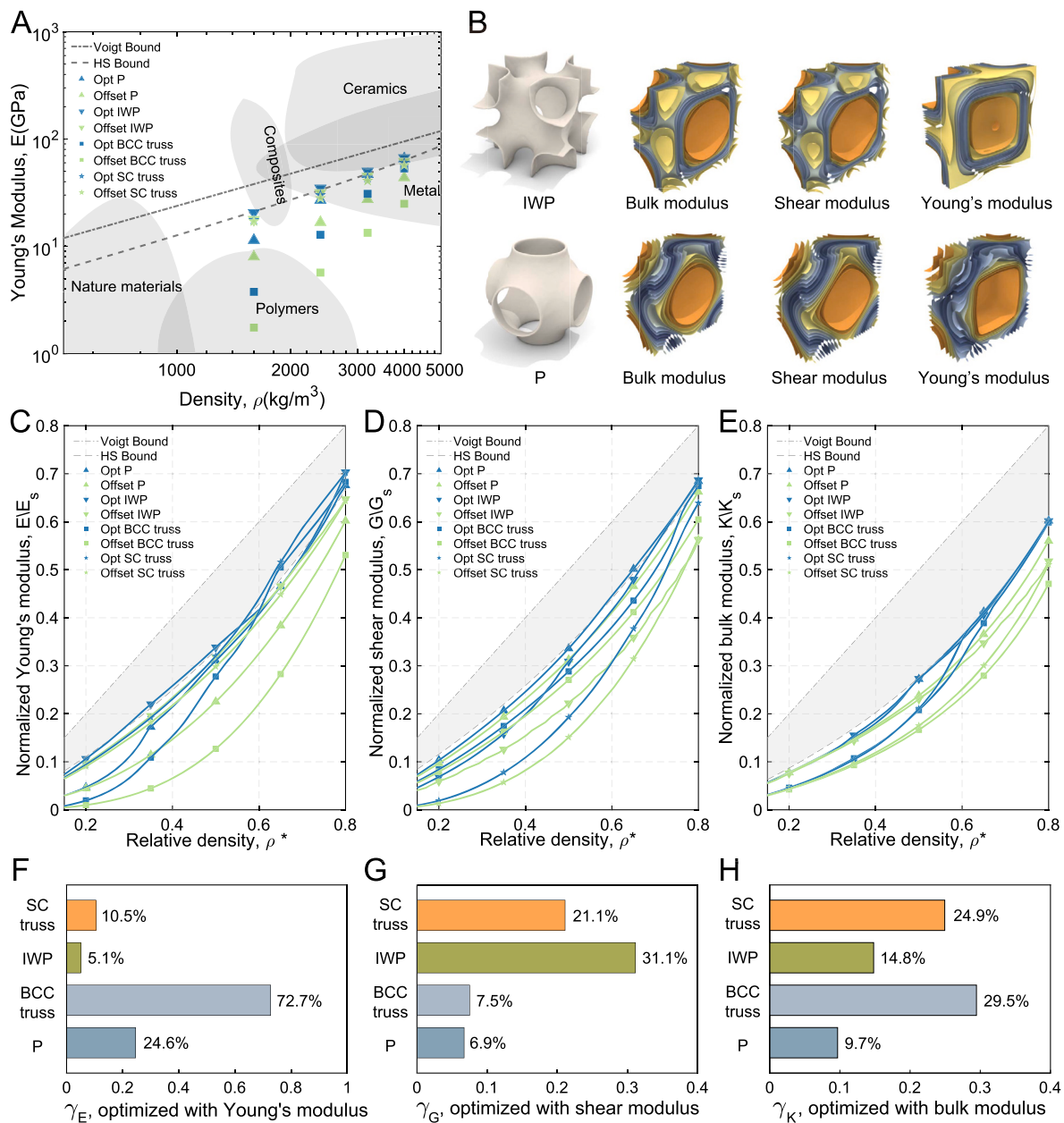
Fig. 3. The optimized microstructure sequence achieves extreme stiffness. A) Comparing the Young's modulus of sequences optimized with Young's modulus as the objective function, utilizing Schwarz P, IWP, BCC truss, and SC (simple cubic) truss as candidate cells, with the Young's modulus of offset sequences within the material property space. SS316L is selected as our constituent material, with Young's modulus and density of 190 GPa and 7990 kg / m^3, respectively. B) Illustrating the isosurfaces of optimized microstructure sequences, using Schwarz P and IWP structures as candidate cells, with bulk modulus, shear modulus, and Young's modulus as objective functions. C-E) Using Young's modulus (C), shear modulus (D), and bulk modulus (E) as objective functions, sequences were optimized employing Schwarz P, IWP, BCC truss, and SC truss as candidate cells. Modulus vs. relative density of the optimized sequences were compared with their corresponding offset sequences. F-H) Histograms depicting the improvement ratio γ_M over four optimized microstructure sequences and their corresponding offset sequences under objective functions related to Young's modulus (F), shear modulus (G), and bulk modulus (H). Here, γ_M is defined as the ratio of the area enclosed by the optimized sequence curve and the x-axis to the area enclosed by the offset sequence curve and the x-axis, when the objective function is the modulus M. M can be E (Young's modulus), G (shear modulus), or K (bulk modulus).

Here, Young's modulus from the simulations was obtained through numerical analysis of the $5 \times 5 \times 5$ array. Details can be found in the supplementary text, Fig. S7 and Fig. S8. The data indicate a close alignment between the experimental and numerical results at a low relative density. However, at a higher relative density (50%), the experimental outcomes approximate 80% of the numerical predictions. This discrepancy is primarily attributed to manufacturing inaccuracies, including thermal distortion [63], which are introduced during the fabrication of metamaterials with high relative densities.

3.3. Topologically enabled material performance

The proposed method is an experience-free and systematic approach for the design of architectured metamaterial sequences. In the course of feature evolution within microstructure sequences that possess a specified modulus, certain topological transformations of structures have also been observed. The identification of these topological features offers valuable insights for the design of more diverse structures.
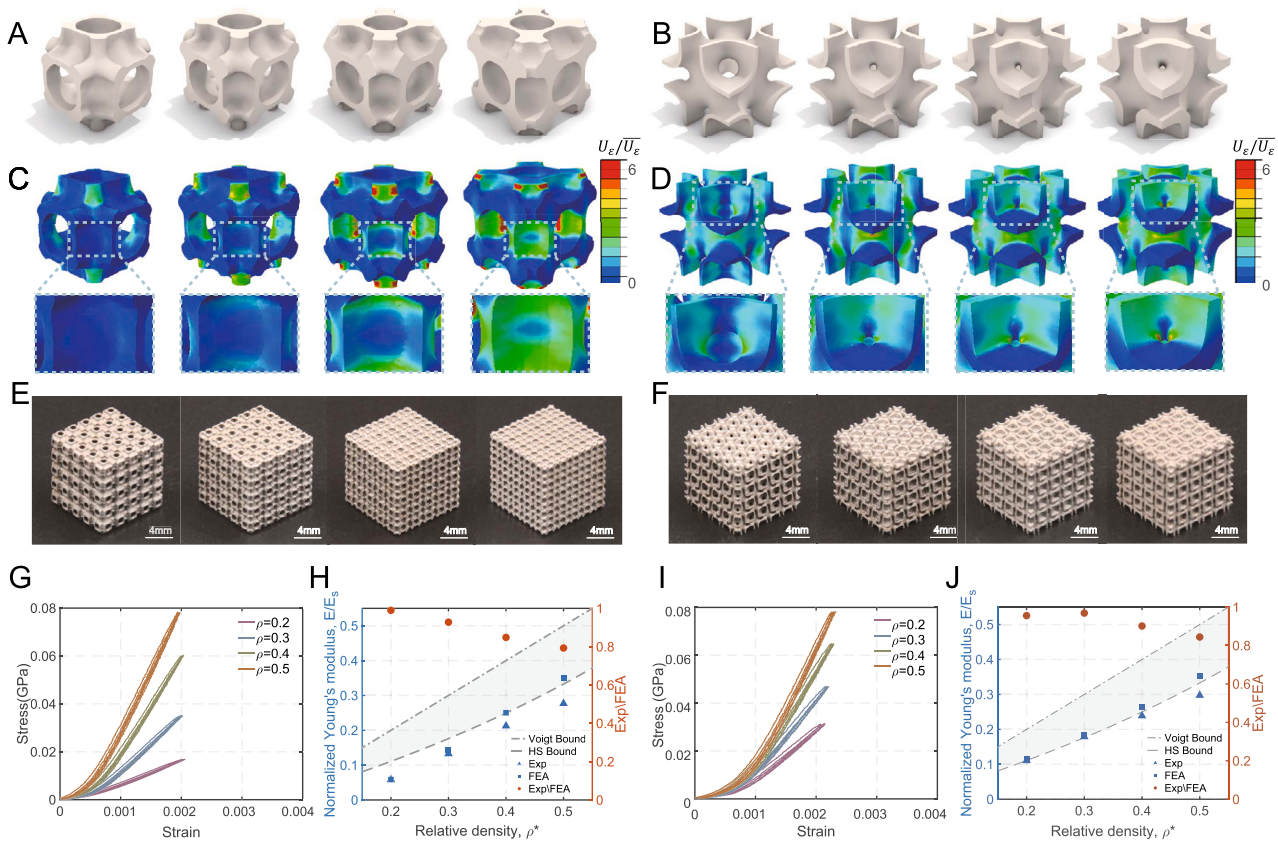
Fig. 4. Simulation and experimental testing of Schwarz P and IWP lattice samples. A,B) Metamaterials from the Opt Schwarz P-Young's sequence (A) and the Opt IWP-Young's sequence (B) at relative densities $\rho^* = 0.2, 0.3, 0.4, 0.5$, respectively referred to as the Schwarz P set and IWP set. C,D) The normalized strain energy density contour plots for the Schwarz P (C) set and IWP set (D) under uniaxial compression along the vertical direction with strain $\varepsilon = 0.001$. E,F) Photos of the fabrication models of the Schwarz P set (E) and IWP set (F), each obtained by arranging corresponding cells in a $5 \times 5 \times 5$ array, with a total size of $15\,mm \times 15\,mm \times 15\,mm$. G) The stress-strain curves of the fabricated models of the Schwarz P set under loading-unloading compression testing. H) The Young's modulus of the fabricated models of the Schwarz P set is calculated from the stress-strain curves, along with a comparison of the results obtained from simulation and experiment. I) and J) respectively refer to the results applied to the IWP set by (G) and (H).

- Topological change. Taking the Opt BCC truss-Young's sequence as an example, the curve of bulk modulus vs. relative density is shown in Fig. 5A. At a relative density of $\rho^* = 0.68$, there is an inflection point. Observing the structure near the inflection point, as shown in Fig. 5B, it can be noted that a topological change appears in the structure, transitioning from an open cell to a closed cell. The same conclusion can be observed in the Opt SC truss-Young's sequence, as shown in Fig. S9. For OCTO, where the objective function is based on Young's modulus, three distinct channel constraints are applied during optimization, leading to the optimization sequences depicted in Fig. 5C. It is evident that OCTO prioritizes the reduction and closure of holes in the corners, while holes in the center of the faces either close later or remain open. In Fig. 5C, the microstructure is annotated with triangles, and simulations are conducted. We selected a representative structure from each of the three optimization sequences, highlighted with different colors in Fig. 5C, and performed numerical simulations on them. The strain energy density contour plot in Fig. 5D reveals that holes in the corners significantly influence the distribution of the strain energy density in those regions. Smaller holes result in higher strain energy in the corners, prompting the algorithm to prioritize closing these holes. On the other hand, holes in the center of the faces have a minimal impact on the distribution of strain energy.
- Geometric change. To investigate the impact of smoothness at joints in the IWP on Young's modulus, we generated IWP structures using two methods: one employing the level-set function method (in Fig. S10) and the other utilizing Surface Evolver software. Both

types of IWP structures are used as candidate cells, subjected to offset operations, and optimized with Young's modulus as the objective function. As depicted in Fig. 5E, Young's modulus of the offset sequence corresponding to the IWP generated by the level-set function method consistently exhibits lower values than the offset sequence generated by the Surface Evolver. However, the optimization sequences of the two types of IWP converge to a similar pattern at high relative densities. Upon analyzing the structures at a relative density of $\rho^* = 0.4$, which are arranged in a $2 \times 2 \times 2$ array, it becomes apparent that the offset sequence of the IWP generated by the level-set function exhibits concavities at the joints, while the offset sequence of the IWP generated by Surface Evolver features smoother joints. Interestingly, both optimization sequences demonstrate smooth joints. This observation suggests that the smoothness of joints can indeed influence Young's modulus, with non-smooth joints leading to lower Young's modulus values. The optimization algorithm seeks to enhance Young's moduli of lattices by increasing the smoothness of their joints.

3.4. Customized modulus

The proposed algorithm allows for customizing objective functions to attain desired mechanical properties. IWP and Schwarz P are chosen as candidate cells, and the optimization is performed with the multi-directional Young's modulus E_M and total stiffness E_T as objective functions. The optimized sequences are compared with those obtained
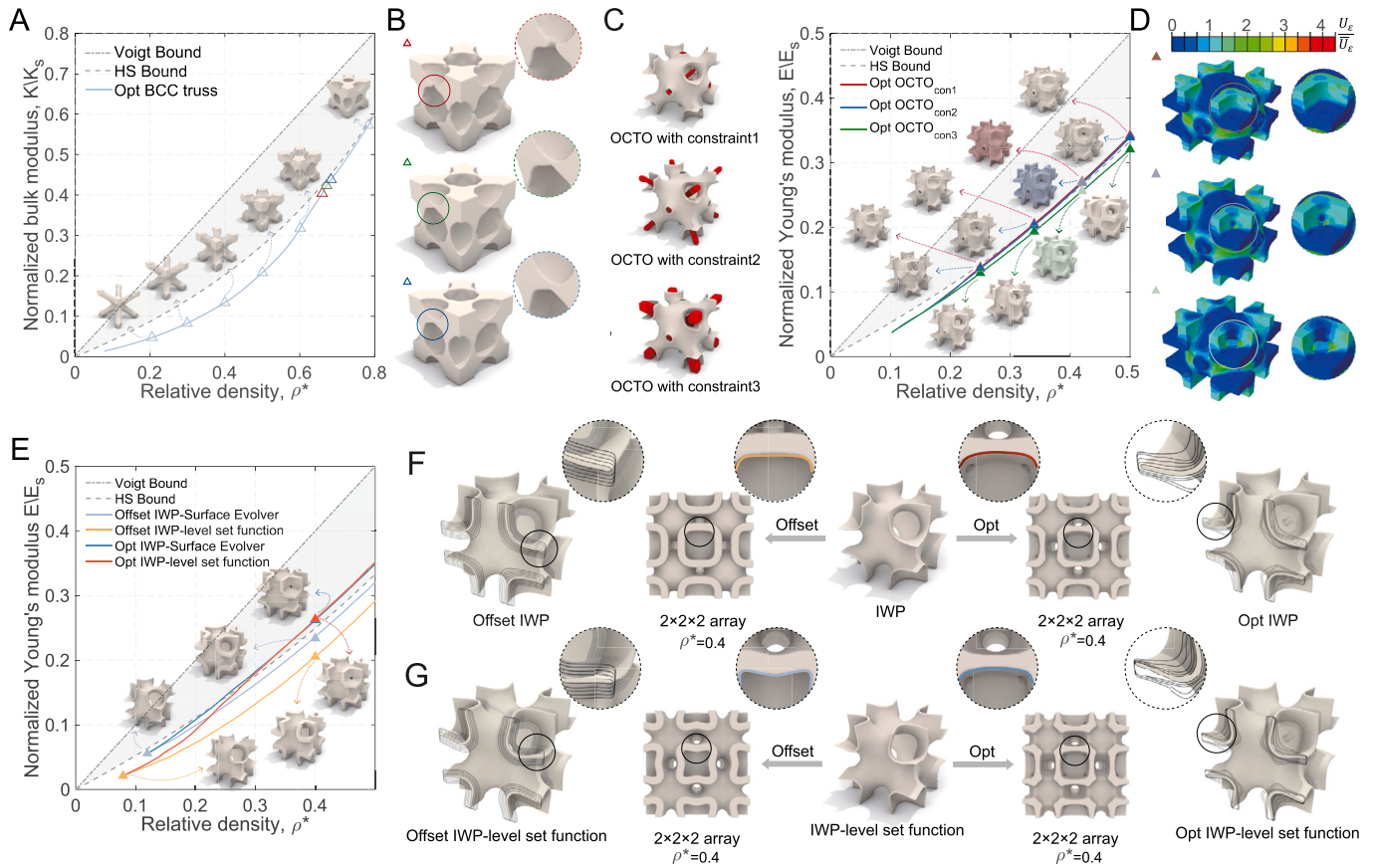
Fig. 5. The mechanisms of topological and geometric variations. A) Plot of bulk modulus vs. relative density for the Opt BCC truss-bulk sequence. B) Details of the topological changes of the metamaterial sequence marked with triangles in (A). C) Plot of Young's modulus vs. relative density for the Opt OCTO-Young's sequences under various channel constraints. D) Strain energy density contour plots for the structure marked with a triangle in (C) under uni-axial stress with strain $\varepsilon = 0.1$. E) Plot of Young's modulus vs. relative density. The IWP structure is the candidate cell generated by two methods: (1) level-set function and (2) Surface Evolver. For the optimized sequences, the objective function is Young's modulus. F,G) Detailed comparisons at the joints of the offset sequences and optimized sequences are shown in (E).

using the uni-axial Young's modulus E_U as the objective function, where E_U represents the Young's modulus in the [100] direction. The expressions for E_M and E_T are given by:

$$E_M = E_{100} + E_{110} + E_{111},$$

$$E_T = (E + 2G(1 - v))/(E_{HS} + 2G_{HS}(1 - v_{HS})),$$

where E_{100}, E_{110}, and E_{111} are Young's modulus in the [100], [110], and [111] directions, respectively. The subscript "HS" denotes the HS upper bound for the corresponding modulus. Fig. 6C and Fig. 6D depict the comparison of Young's modulus (E) in three directions between the optimization sequences targeting the uni-axial Young's modulus and those with the multi-directional Young's modulus. It is evident that Young's modulus in the [100] direction of the sequence optimized with the multi-directional Young's modulus as the objective function is smaller than that of the sequence optimized with uni-axial Young's modulus as the objective function, whereas in the [110] and [111] directions, it is greater. This arises from the optimization of the multi-directional Young's modulus, where the optimized sequence achieves a balance across the Young's moduli in three directions. Consequently, the obtained sequence may demonstrate diminished performance in Young's modulus along the [100] direction compared to a sequence optimized solely for uniaxial Young's modulus, while exhibiting increased stiffness in the remaining two directions. Concerning the total stiffness as the objective function, it is notable that the Opt Schwarz P-E_T sequence exhibits a lower Young's modulus than the Opt Schwarz P-E_U sequence. However, the shear modulus and bulk modulus are greater. Total stiff-

ness provides a comprehensive evaluation of each modulus, resulting in a sequence optimized to be more balanced across different uni-axial Young's modulus performances compared to sequences optimized with the uni-axial Young's modulus as the objective function. In the case of the IWP, the performances of the two optimization sequences are generally similar across the three moduli. This might be attributed to the lower degree of anisotropic elasticity in the IWP structure.

3.5. Isotropy properties

To achieve microstructure sequences approaching isotropy, isotropy constraints are integrated into the framework. We select the cubic-octet plate [22], the SC-BCC plate [24], and the isotropic truss [35] at low relative densities as candidate cells. They are then optimized with Young's modulus as the objective, and isotropy constraints are applied. The diameter ratios between the different constituents of the three structures are illustrated in Fig. 7A-C. Microstructure sequences conforming to these ratios are considered as benchmark sequences and compared with our optimized sequences. For the cubic-octet plate and SC-BCC plate, the zener ratio of the optimized sequences remains close to 1, indicating preserved isotropy. However, the increase in Young's modulus of the optimized sequences compared to the benchmark sequences is relatively small. This is because the cubic-octet plate and SC-BCC plate structures already possess extremely high stiffness and isotropy, resulting in a limited optimization space. Moreover, based on voxel representation, our framework cannot accurately replicate the thickness ratios between different plates, leading to limited improvements in our optimization
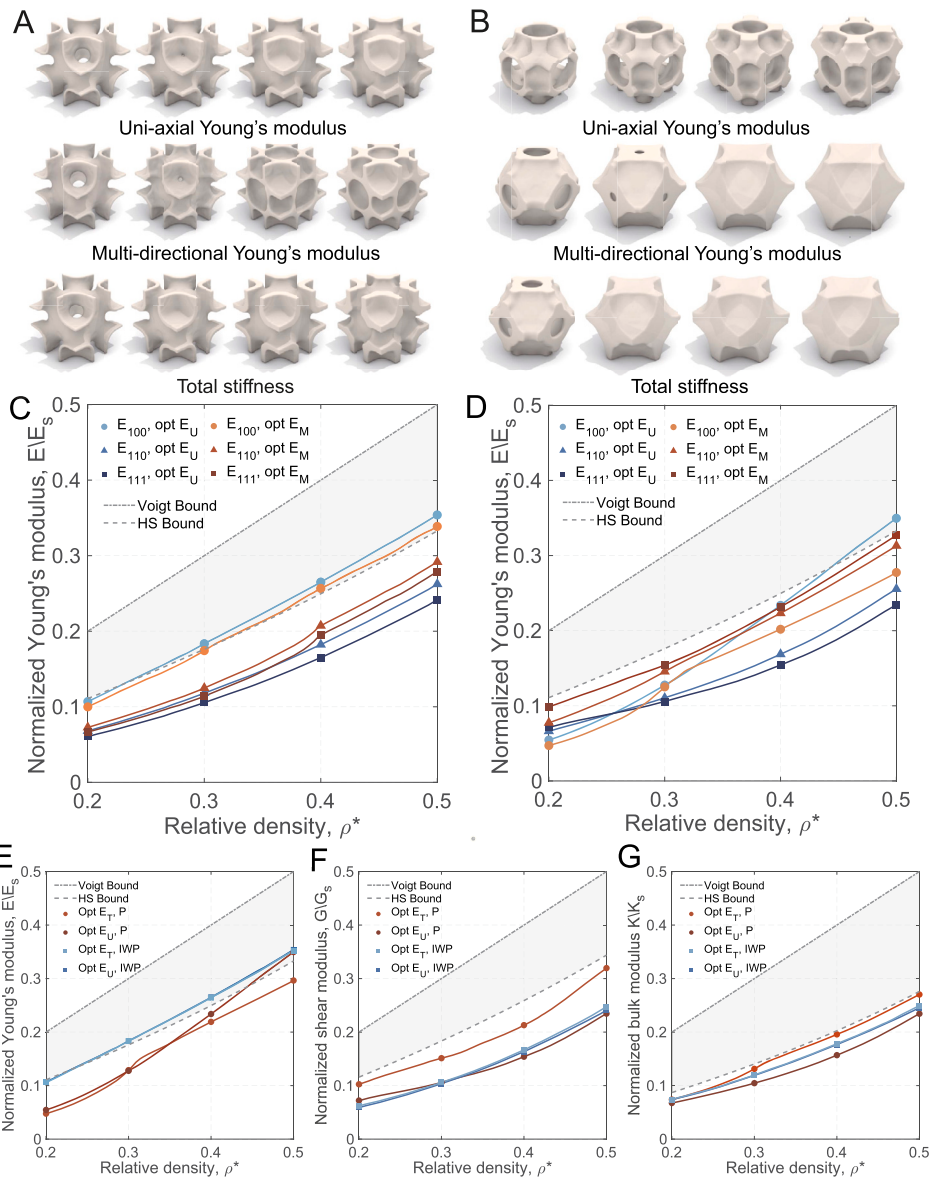
Fig. 6. Customized mechanical behavior. A,B) Optimized metamaterial sequences from IWP (A) and Schwarz P (B) with different objective functions: uni-axial Young's modulus, multi-directional Young's modulus, and total stiffness. C,D) Comparison of Young's modulus values in three directions for optimized metamaterial sequences from IWP (C) and Schwarz P (D) using uniaxial Young's modulus and the sum of Young's modulus in the [100], [110], and [111] directions as objective functions. E-G) Comparison of Young's modulus (E), shear modulus (F), and bulk modulus (G) for optimized metamaterial sequences from IWP and Schwarz P with uni-axial Young's modulus and total stiffness as the objective functions.

results. As for the isotropic truss, our optimized sequences exhibit a significant enhancement in Young's modulus compared to the benchmark sequences, and the zener ratio consistently approaches 1.

To further demonstrate the effectiveness of our framework in terms of isotropy constraints, we utilized IWP and Schwarz P structures as candidate cells, incorporated isotropy constraints, and optimized Young's modulus. As shown in Fig. 8, the optimized sequences of Schwarz P and IWP exhibit zener ratios close to 1, indicating higher isotropy compared to the offset sequences. This is also evident in Young's modulus, as the optimized sequences show similar values for Young's modulus in both the [100] and [111] directions. Moreover, for the Schwarz P structure, at a relative density of 0.48, the optimized sequence's Young's modulus surpasses that of the Offset sequence in the [111] direction, where the [111] direction corresponds to the highest Young's modulus for the Schwarz P structure.

4. Conclusion

Our framework can be used to precisely tailor the properties of metamaterial sequences while approaching extreme stiffness. We integrate shape optimization based on the candidate cell into the thermal diffusion process, resulting in several benefits. Firstly, our algorithm can rapidly generate a metamaterial sequence for a given candidate cell that improves the specific modulus. For instance, the Opt IWP-Young's sequences reach the HS upper bound of Young's modulus at a relative density of 0.24, outperforming previous works [4,64]. Moreover, compared to inverse design based on parameterized approaches [65], our voxel-based representation provides higher optimization freedom and larger design space, enabling more refined control during the optimization process. Secondly, despite optimizing for extreme stiffness, our method can also customize other mechanical properties for inverse design, such as total stiffness and isotropy. Unlike works [22,24] that rely on proportional regulation, we incorporate isotropy constraints directly
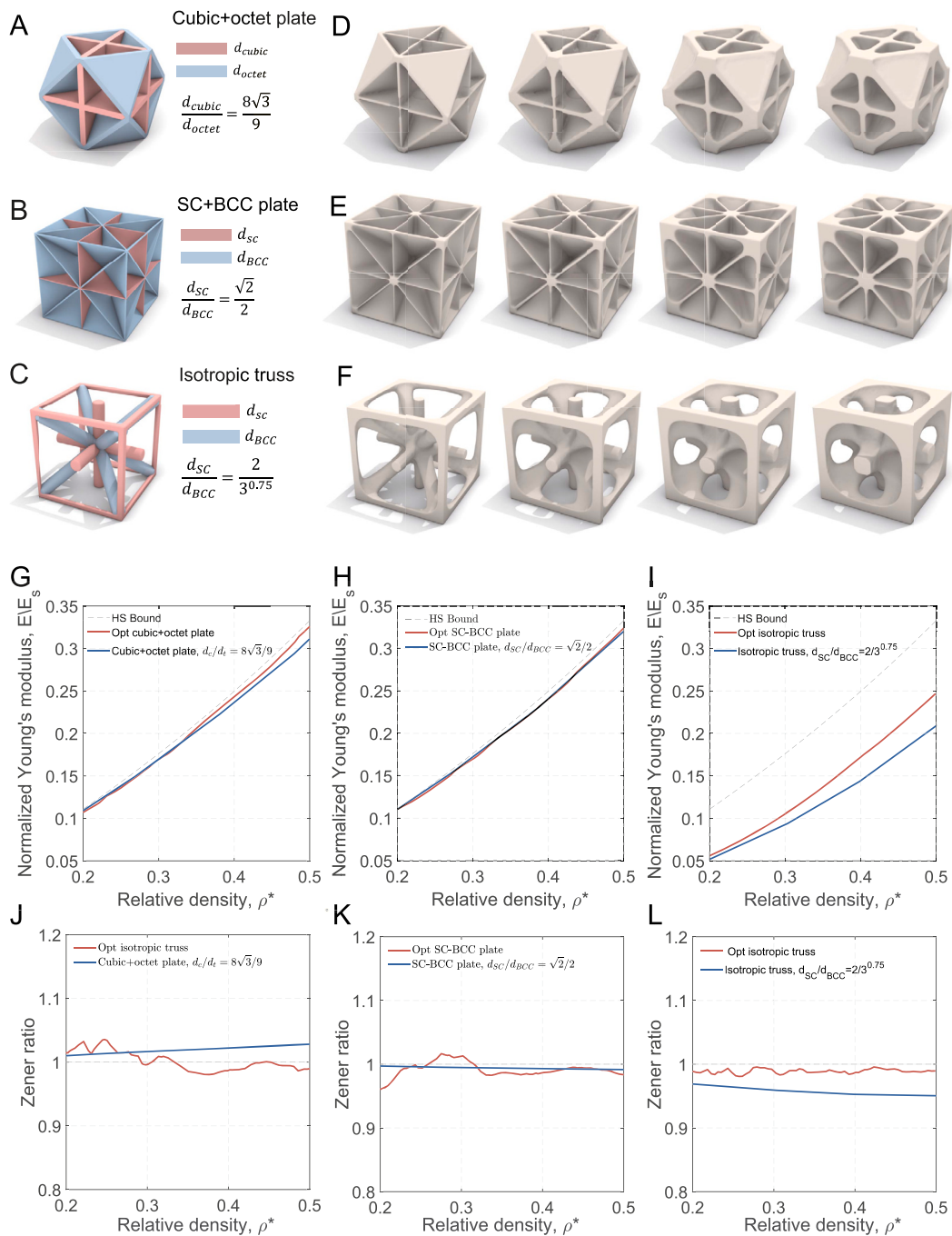
Fig. 7. Optimization of isotropic candidate cells with isotropy constraints. Optimizing with isotropy constraints using cubic-octet plate, SC-BCC plate, and isotropic truss as candidate cells, with Young's modulus as the objective function. A-C) The composition of the benchmark cubic+octet plate (A), the benchmark SC-BCC plate (B), and the benchmark isotropic truss (C). D-F) Optimization sequence of cubic+octet plate (D), SC-BCC plate (E), and isotropic truss (F). In each row, the relative densities of the four structures from left to right are 0.2, 0.3, 0.4, and 0.5. G-I) Comparison of the Young's modulus between the benchmark sequences and the optimized sequences for the three models. J-L) Comparison of the zener ratio between the benchmark sequences and the optimized sequences for the three models.

into the inverse design process. Finally, the continuous microstructure sequence generated by our framework allows for a continuous mapping between relative density and modulus, offering distinct advantages in multiscale design. This expands the design space compared to discrete microstructures [57]. When integrated into multiscale structures, the geometric transformations alleviate stress concentration and address connectivity issues between microstructure units, further demonstrating the robustness and adaptability of our algorithm across diverse scenarios. However, its limitation lies in the need to predefine the candidate cell, which cannot be dynamically modified during the optimization process.

CRediT authorship contribution statement

Jiacheng Han: Writing – review & editing, Writing – original draft, Visualization, Validation, Methodology. **Xiaoya Zhai:** Writing – review & editing, Writing – original draft, Visualization, Validation, Supervision, Methodology, Conceptualization. **Lili Wang:** Writing – review & editing, Visualization, Validation. **Di Zhang:** Validation, Conceptualization. **Junhao Ding:** Visualization, Validation. **Winston Wai Shing Ma:** Writing – review & editing, Visualization, Supervision, Resources, Conceptualization. **Xu Song:** Funding acquisition, Data curation, Conceptualization. **Wei-Hsin Liao:** Validation, Supervision, Conceptualization.
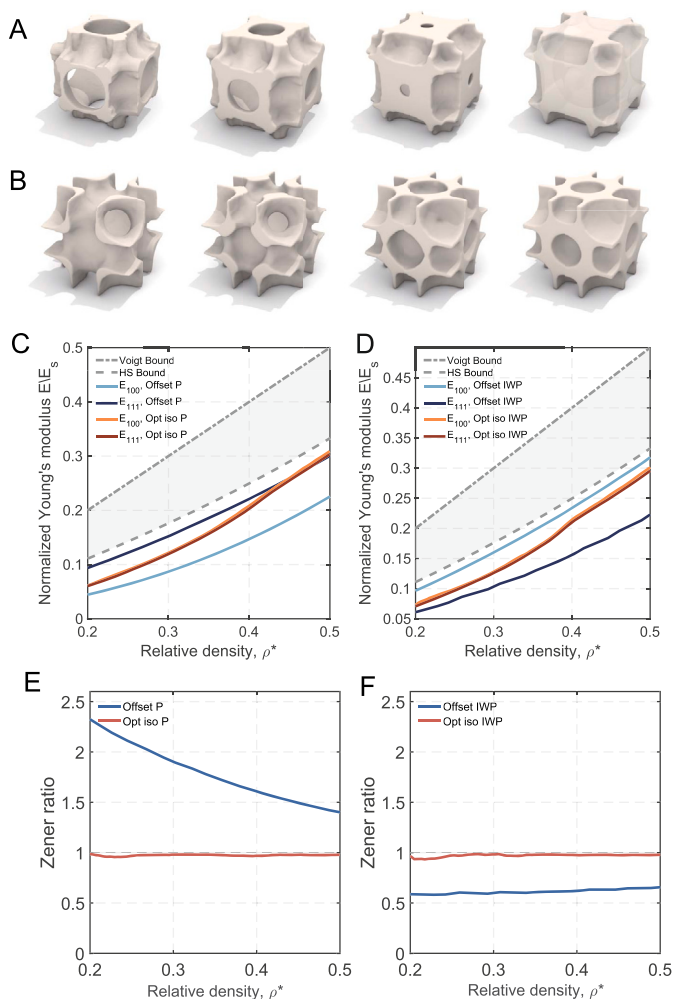
Fig. 8. Optimization of Schwarz P and IWP with isotropy constraints. Optimizing with isotropy constraints using Schwarz P and IWP as candidate cells, with Young's modulus as the objective function. A and B) Optimization sequence of Schwarz P (A) and IWP (B). In each row, the relative densities of the four structures from left to right are 0.2, 0.3, 0.4, and 0.5. C and D) Comparison of Young's modulus between the offset sequences and the optimized sequences for Schwarz P (C) and IWP (D). E and F) Comparison of the zener ratio between the offset sequences and the optimized sequences for Schwarz P (E) and IWP (F).

Ligang Liu: Writing – review & editing, Visualization, Conceptualization. **Jun Wu:** Validation, Supervision, Methodology, Conceptualization. **Xiao-Ming Fu:** Writing – review & editing, Writing – original draft, Visualization, Validation, Supervision, Methodology, Investigation, Conceptualization.

Declaration of competing interest

The authors declare that they have no known competing financial interests or personal relationships that could have appeared to influence the work reported in this paper.

Acknowledgement

Appendix A. Supplementary material

Supplementary material related to this article can be found online at https://doi.org/10.1016/j.matdes.2024.113350.

Data availability

The data for this paper is at https://github.com/JiachengHan1025/Inverse3Dmetamaterials.

References

[1] X. Zhang, A. Vyatskikh, H. Gao, J.R. Greer, X. Li, Lightweight, flaw-tolerant, and ultrastrong nanoarchitected carbon, Proc. Natl. Acad. Sci. 116 (14) (2019) 6665–6672.

[2] X. Zheng, H. Lee, T.H. Weisgraber, M. Shusteff, J. DeOtte, E.B. Duoss, J.D. Kuntz, M.M. Biener, Q. Ge, J.A. Jackson, et al., Ultralight, ultrastiff mechanical metamaterials, Science 344 (6190) (2014) 1373–1377.

[3] H. Cui, R. Hensleigh, D. Yao, D. Maurya, P. Kumar, M.G. Kang, S. Priya, X. Zheng, Three-dimensional printing of piezoelectric materials with designed anisotropy and directional response, Nat. Mater. 18 (3) (2019) 234–241.

[4] Y. Wang, X. Zhang, Z. Li, H. Gao, X. Li, Achieving the theoretical limit of strength in shell-based carbon nanolattices, Proc. Natl. Acad. Sci. 119 (34) (2022) e2119536119.

[5] Z. Vangelatos, H.M. Sheikh, P.S. Marcus, C.P. Grigoropoulos, V.Z. Lopez, G. Flamourakis, M. Farsari, Strength through defects: a novel Bayesian approach for the optimization of architected materials, Sci. Adv. 7 (41) (2021) eabk2218.

[6] S. Yuan, C.K. Chua, K. Zhou, 3d-printed mechanical metamaterials with high energy absorption, Adv. Mater. Technol. 4 (3) (2019) 1800419.

[7] T. Meier, R. Li, S. Mavrikos, B. Blankenship, Z. Vangelatos, M.E. Yildizdag, C.P. Grigoropoulos, Obtaining auxetic and isotropic metamaterials in counterintuitive design spaces: an automated optimization approach and experimental characterization, npj Comput. Mater. 10 (1) (2024) 3.

[8] H.M. Sheikh, T. Meier, B. Blankenship, Z. Vangelatos, N. Zhao, P.S. Marcus, C.P. Grigoropoulos, Systematic design of Cauchy symmetric structures through Bayesian optimization, Int. J. Mech. Sci. 236 (2022) 107741.

[9] J. Ding, Q. Ma, X. Li, L. Zhang, H. Yang, S. Qu, M.Y. Wang, W. Zhai, H. Gao, X. Song, Imperfection-enabled strengthening of ultra-lightweight lattice materials, Adv. Sci. (2024) 2402727.

[10] S. Zhao, Y. Zhang, H. Wu, Y. Zhang, J. Yang, Functionally graded graphene origami-enabled auxetic metamaterial beams with tunable buckling and postbuckling resistance, Eng. Struct. 268 (2022) 114763.

[11] Z. Zhang, L. Zhang, B. Song, Y. Yao, Y. Shi, Bamboo-inspired, simulation-guided design and 3d printing of light-weight and high-strength mechanical metamaterials, Appl. Mater. Today 26 (2022) 101268.

[12] Z. Vangelatos, M.E. Yildizdag, C.P. Grigoropoulos, A designer's challenge: unraveling the architected structure of deep sea sponges for lattice mechanical metamaterials, Extrem. Mech. Lett. 61 (2023) 102013.

[13] L. Xia, P. Breitkopf, Design of materials using topology optimization and energy-based homogenization approach in Matlab, Struct. Multidiscip. Optim. 52 (6) (2015) 1229–1241.

[14] H.T. Kollmann, D.W. Abueidda, S. Koric, E. Guleryuz, N.A. Sobh, Deep learning for topology optimization of 2d metamaterials, Mater. Des. 196 (2020) 109098.

[15] L. Wang, J. Boddapati, K. Liu, P. Zhu, C. Daraio, W. Chen, Mechanical cloak via data-driven aperiodic metamaterial design, Proc. Natl. Acad. Sci. 119 (13) (2022) e2122185119.

[16] W. Yang, Q. Liu, Z. Gao, Z. Yue, B. Xu, Theoretical search for heterogeneously architected 2d structures, Proc. Natl. Acad. Sci. 115 (31) (2018) E7245–E7254.

[17] H.-W. Dong, S.-D. Zhao, X.-B. Miao, C. Shen, X. Zhang, Z. Zhao, C. Zhang, Y.-S. Wang, L. Cheng, Customized broadband pentamode metamaterials by topology optimization, J. Mech. Phys. Solids 152 (2021) 104407.

[18] X. Lin, F. Pan, K. Yang, J. Guan, B. Ding, Y. Liu, K. Yang, B. Liu, Y. Chen, A stair-building strategy for tailoring mechanical behavior of re-customizable metamaterials, Adv. Funct. Mater. 31 (37) (2021) 2101808.

[19] Z. Meng, M. Liu, H. Yan, G.M. Genin, C.Q. Chen, Deployable mechanical metamaterials with multistep programmable transformation, Sci. Adv. 8 (23) (2022) eabn5460.

[20] H. Zhang, X. Guo, J. Wu, D. Fang, Y. Zhang, Soft mechanical metamaterials with unusual swelling behavior and tunable stress-strain curves, Sci. Adv. 4 (6) (2018) eaar8535.

[21] A. Clausen, F. Wang, J.S. Jensen, O. Sigmund, J.A. Lewis, Topology optimized architectures with programmable Poisson's ratio over large deformations, Adv. Mater. 27 (37) (2015) 5523–5527.

[22] J. Berger, H. Wadley, R. McMeeking, Mechanical metamaterials at the theoretical limit of isotropic elastic stiffness, Nature 543 (7646) (2017) 533–537.

[23] Y. Liu, Mechanical properties of a new type of plate–lattice structures, Int. J. Mech. Sci. 192 (2021) 106141.

[24] T. Tancogne-Dejean, M. Diamantopoulou, M.B. Gorji, C. Bonatti, D. Mohr, 3d plate-lattices: an emerging class of low-density metamaterial exhibiting optimal isotropic stiffness, Adv. Mater. 30 (45) (2018) 1803334.

[25] D. Chen, M. Skouras, B. Zhu, W. Matusik, Computational discovery of extremal microstructure families, Sci. Adv. 4 (1) (2018) eaao7005.

[26] O. Al-Ketan, R. Rezgui, R. Rowshan, H. Du, N.X. Fang, R.K. Abu Al-Rub, Microarchitected stretching-dominated mechanical metamaterials with minimal surface topologies, Adv. Eng. Mater. 20 (9) (2018) 1800029.

[27] N. Kladovasilakis, K. Tsongas, I. Kostavelis, D. Tzovaras, D. Tzetzis, Effective mechanical properties of additive manufactured strut-lattice structures: experimental and finite element study, Adv. Eng. Mater. 24 (3) (2022) 2100879.

[28] A.G. Evans, J.W. Hutchinson, N.A. Fleck, M. Ashby, H. Wadley, The topological design of multifunctional cellular metals, Prog. Mater. Sci. 46 (3–4) (2001) 309–327.

[29] P. Fratzl, R. Weinkamer, Nature's hierarchical materials, Prog. Mater. Sci. 52 (8) (2007) 1263–1334.

[30] Q. Ma, H. Cheng, K.-I. Jang, H. Luan, K.-C. Hwang, J.A. Rogers, Y. Huang, Y. Zhang, A nonlinear mechanics model of bio-inspired hierarchical lattice materials consisting of horseshoe microstructures, J. Mech. Phys. Solids 90 (2016) 179–202.

[31] A.M. Torres, A.A. Trikanad, C.A. Aubin, F.M. Lambers, M. Luna, C.M. Rimnac, P. Zavattieri, C.J. Hernandez, Bone-inspired microarchitectures achieve enhanced fatigue life, Proc. Natl. Acad. Sci. 116 (49) (2019) 24457–24462.

[32] M.-S. Pham, C. Liu, I. Todd, J. Lertthanasarn, Damage-tolerant architected materials inspired by crystal microstructure, Nature 565 (7739) (2019) 305–311.

[33] B. Deng, G.J. Cheng, Soap film inspired mechanical metamaterials approaching theoretical bound of stiffness across full density range, Mater. Horiz. 8 (3) (2021) 987–996.

[34] Y. Wang, F. Xu, H. Gao, X. Li, Elastically isotropic truss-plate-hybrid hierarchical microlattices with enhanced modulus and strength, Small (2023) 2206024.

[35] M.C. Messner, Optimal lattice-structured materials, J. Mech. Phys. Solids 96 (2016) 162–183.

[36] J. Du, Y. Liu, Y. Wang, H. Ren, Z. Meng, X. Chen, Z. Li, L. Wang, W. Chen, Y. Wang, Achieving extreme stiffness for beam-plate-shell-combined lattice metamaterial through a multilayer strategy and topology optimization, arXiv preprint, arXiv:2301.08911, 2023.

[37] M.P. Bendsøe, Optimal shape design as a material distribution problem, Struct. Optim. 1 (1989) 193–202.

[38] M.Y. Wang, X. Wang, D. Guo, A level set method for structural topology optimization, Comput. Methods Appl. Mech. Eng. 192 (1–2) (2003) 227–246.

[39] J.A. Sethian, A. Wiegmann, Structural boundary design via level set and immersed interface methods, J. Comput. Phys. 163 (2) (2000) 489–528.

[40] X. Guo, W. Zhang, W. Zhong, Doing topology optimization explicitly and geometrically—a new moving morphable components based framework, J. Appl. Mech. 81 (8) (2014) 081009.

[41] H.A. Eschenauer, N. Olhoff, Topology optimization of continuum structures: a review, Appl. Mech. Rev. 54 (4) (2001) 331–390.

[42] O. Sigmund, K. Maute, Topology optimization approaches: a comparative review, Struct. Multidiscip. Optim. 48 (6) (2013) 1031–1055.

[43] O. Sigmund, M. Bondsgc, Topology Optimization, State-of-the-Art and Future Perspectives, Technical University of Denmark (DTU), Copenhagen, 2003.

[44] D. Zhang, X. Zhai, L. Liu, X.-M. Fu, An optimized, easy-to-use, open-source gpu solver for large-scale inverse homogenization problems, arXiv preprint, arXiv:2301.08911, 2023.

[45] X. Zheng, X. Zhang, T.-T. Chen, I. Watanabe, Deep learning in mechanical metamaterials: from prediction and generation to inverse design, Adv. Mater. 35 (45) (2023) 2302530.

[46] D. Lee, W. Chen, L. Wang, Y.-C. Chan, W. Chen, Data-driven design for metamaterials and multiscale systems: a review, Adv. Mater. 36 (8) (2024) 2305254.

[47] H. Peng, A. Liu, J. Huang, L. Cao, J. Liu, L. Lu, Ph-net: parallelepiped microstructure homogenization via 3d convolutional neural networks, Addit. Manuf. 60 (2022) 103237.

[48] J.-H. Bastek, D.M. Kochmann, Inverse design of nonlinear mechanical metamaterials via video denoising diffusion models, Nat. Mach. Intell. 5 (12) (2023) 1466–1475.

[49] Y. Yang, L. Wang, X. Zhai, K. Chen, W. Wu, Y. Zhao, L. Liu, X.-M. Fu, Guided diffusion for fast inverse design of density-based mechanical metamaterials, arXiv preprint, arXiv:2401.13570, 2024.

[50] Z. Chen, Y.M. Xie, X. Wu, Z. Wang, Q. Li, S. Zhou, On hybrid cellular materials based on triply periodic minimal surfaces with extreme mechanical properties, Mater. Des. 183 (2019) 108109.

[51] T. Li, F. Jarrar, R.A. Al-Rub, W. Cantwell, Additive manufactured semi-plate lattice materials with high stiffness, strength and toughness, Int. J. Solids Struct. 230 (2021) 111153.

[52] M.J. Baishya, B.J. Sahariah, N. Muthu, P. Khanikar, Composite strut-plate lattice: a high-stiffness design of cellular metamaterial having excellent strength and energy absorption ability, Mater. Today Commun. 33 (2022) 104939.

[53] S.T. Zobaer, A. Sutradhar, An energy-based method for interface connectivity of incompatible microstructures through parametric modeling, Comput. Methods Appl. Mech. Eng. 370 (2020) 113278.

[54] Y. Zhang, M. Xiao, L. Gao, J. Gao, H. Li, Multiscale topology optimization for minimizing frequency responses of cellular composites with connectable graded microstructures, Mech. Syst. Signal Process. 135 (2020) 106369.

[55] E. Sanders, A. Pereira, G. Paulino, Optimal and continuous multilattice embedding, Sci. Adv. 7 (16) (2021) eabf4838.

[56] A.D. Cramer, V.J. Challis, A.P. Roberts, Microstructure interpolation for macroscopic design, Struct. Multidiscip. Optim. 53 (2016) 489–500.

[57] E. Garner, H.M. Kolken, C.C. Wang, A.A. Zadpoor, J. Wu, Compatibility in microstructural optimization for additive manufacturing, Addit. Manuf. 26 (2019) 65–75.

[58] X. Cheng, C. Liu, W. Zhang, Z. Tang, Y. Liu, S. Tang, Z. Du, T. Cui, X. Guo, A compatible boundary condition-based topology optimization paradigm for static mechanical cloak design, Extrem. Mech. Lett. 65 (2023) 102100.

[59] Z.a. Hashin, S. Shtrikman, On some variational principles in anisotropic and nonhomogeneous elasticity, J. Mech. Phys. Solids 10 (4) (1962) 335–342.

[60] K.A. Brakke, The surface evolver, Exp. Math. 1 (2) (1992) 141–165.

[61] S.L. Omairey, P.D. Dunning, S. Sriramula, Development of an abaqus plugin tool for periodic rve homogenisation, Eng. Comput. 35 (2019) 567–577.

[62] X. Yu, F. Wang, Z. Luo, Z. Kang, Y. Wang, Design of hierarchical microstructures with isotropic elastic stiffness, Mater. Des. 229 (2023) 111895.

[63] A. Takezawa, Q. Chen, A.C. To, Optimally variable density lattice to reduce warping thermal distortion of laser powder bed fusion, Addit. Manuf. 48 (2021) 102422.

[64] R.K. Abu Al-Rub, D.-W. Lee, K.A. Khan, A.N. Palazotto, Effective anisotropic elastic and plastic yield properties of periodic foams derived from triply periodic Schoen's i-wp minimal surface, J. Eng. Mech. 146 (5) (2020) 04020030.

[65] P. Liu, B. Sun, J. Liu, L. Lu, Parametric shell lattice with tailored mechanical properties, Addit. Manuf. 60 (2022) 103258.